The Effects of Organ-based Tube Current Modulation on Radiation Dose and Image Quality in Computed Tomography Imaging

Diksha Gandhi
Marquette University

THE EFFECTS OF ORGAN-BASED TUBE CURRENT MODULATION ON RADIATION DOSE AND IMAGE QUALITY IN COMPUTED TOMOGRAPHY IMAGING

by

Diksha Gandhi

A Thesis submitted to the Faculty of the Graduate School,
Marquette University,
in Partial Fulfillment of the Requirements for
the Degree of Master of Science

Milwaukee, Wisconsin

August 2014

ABSTRACT
THE EFFECTS OF ORGAN-BASED TUBE CURRENT MODULATION
ON RADIATION DOSE AND IMAGE QUALITY
IN COMPUTED TOMOGRAPHY IMAGING

Diksha Gandhi

Marquette University, 2014

The purpose of this thesis was to quantify dose and noise performance of organ-dose-based tube current modulation (ODM) through experimental studies with an anthropomorphic phantom and simulations with a voxelized phantom library. Tube current modulation is a dose reduction technique that modulates radiation dose in angular and/or slice directions based on patient attenuation. ODM technique proposed by GE Healthcare further reduces tube current for anterior source positions, without increasing current for posterior positions.

Axial CT scans at 120 kV were performed on head and chest phantoms (Rando Alderson Research Laboratories, Stanford, CA) on an ODM-equipped scanner (Optima CT660, GE Healthcare, Chalfont St Giles, England). Dosimeters quantified dose to breast, lung, heart, spine, eye lens and brain regions (mobile MOSFET Dosimetry System, Best Medical, Ottawa, Canada) for ODM, AutomA (z-axis modulation), and SmartmA (angular and z-axis modulation) settings. Noise standard deviation was calculated in brain and chest regions of reconstructed images. To study a variety of patient sizes, Monte Carlo dose simulations, validated with experimental data, were performed on voxelized head and chest phantoms.

Experimental studies on anthropomorphic chest and head phantoms demonstrated reduction in dose at all dosimeter locations with respect to SmartmA, with dose changes of -31.3% (breast), -20.7% (lung), -24.4% (heart), -5.9% (spine), -18.9% (eye), and -10.1% (brain). Simulation studies using voxelized phantoms indicated average dose changes of -33.4% (breast), -20.2% (lung), -18.6% (spine), -20.0% (eye) and -7.2% (brain). ODM reduced dose to the brain and lung tissues, however these tissues would experience up to 15.2% and 13.1% dose increase respectively at noise standard deviation equal to SmartmA. ODM reduced dose to the eye lens in 22 of 28 phantoms (-1.2% to -12.4%), had no change in dose for one phantom, and increased dose for four phantoms (0.7% to 2.3%) with respect to SmartmA at equal noise standard deviation. All phantoms demonstrated breast dose reduction (-2.1% to -27.6%) at equal noise standard deviation. Experimental and simulation studies over a range of patient sizes indicate that ODM has the potential to reduce dose to radiosensitive organs by 5 - 38% with a limited increase in image noise.

ACKNOWLEDGEMENTS

Diksha Gandhi

I would like to sincerely thank my advisor, Dr. Taly Gilat-Schmidt for her constant support and encouragement throughout this journey. This work has been possible due to her tireless efforts in providing me with the right directions to pursue this project, and her tenacious belief in my abilities as a biomedical engineer.

I thank Grant M. Stevens and Dominic Crotty at GE Healthcare, Waukesha, WI for their continuing support, advice and cooperation with experimental studies. I extend my deepest gratitude to my committee member, professor and role model, Dr. Kristina Ropella, for her inspiring words and confidence in me that has always kept me motivated to pursue my passion in engineering. I would like to also thank Dr. Xizhou Feng for his assistance with the use of Père cluster at Marquette.

My parents and my brother for being my backbone, and for trusting me in my every decision — I would have never been able to accomplish anything without their timeless love, generosity and support. For whose continual presence was felt by me even when she was three continents away through her unconditional love, countless sacrifices, and selfless support, I thank my greatest believer, my mom.

This work was funded in part by GE Healthcare, Waukesha, WI. The computing resources were funded in part by NSF Award OCI-0923037.

TABLE OF CONTENTS

LIST OF TABLES

LIST OF FIGURES

CHAPTER 1

Introduction

Statement of the Problem

Approximately 70 million CT scans are performed annually in the United States [1], accounting for an increase by 23 times in the last three decades [2]. Recent advances in CT, including better image quality and reduced acquisition time, have facilitated an exponential growth in its clinical use over the past few years [3]. However, the Food and Drug Administration (FDA) estimates that an adult's risk of developing cancer through radiation dose of one CT scan with an effective dose of more than 10 millisieverts (mSv) is 1 in 2000 [4]. Moreover, the risk of breast cancer is doubled for women receiving two or more CT scans before the age of 23 [5]. In addition to the stochastic risks mentioned above, x-ray radiation also has a deterministic effect on the eye lens during head CT scans, with a threshold of 0.5 Gy suggested for cataract formation for acute, fractionated and chronic exposures [6]. Risk models developed by the BEIR VII committee estimate that lifetime attributable risks of cancer incidence is greater in women and children for all types of cancers and decreases non-linearly with age, therefore concluding the strong dependence of cancer risk on age and sex of patients [7]. Despite the risks involved, CT use is expected to continuously increase especially due to the recent initiation of screening programs recommended for asymptomatic patients for colonoscopy, lung and cardiac screening, as well as whole-body screening [8].

The amount of absorbed radiation dose may vary from patient to patient depending on patient size, type of CT procedure and type of CT scanner used. Due to the adverse radiation effects, various dose reduction techniques have been studied with the objective to minimize the health risks involved with radiation while also maintaining the diagnostic utility of the acquired images. Some of the dose reduction techniques that have been implemented clinically include minimizing the scan range, using automatic exposure control and optimizing the system parameters [9].

Dose modulation (also known as tube current modulation (TCM) or automatic exposure control) is a dose reduction method that modifies tube current, and therefore the x-ray flux, based on varying attenuation in the angular and slice directions [3, 10]. Generally, x-ray scouts acquired prior to the CT scan are used to determine the tube current variation for each rotation. The tube current-time product is then calculated based on the scouts and the image quality requirements specified by the end user. Organ-based tube current modulation (ODM) is an addition to the TCM technique proposed by GE Healthcare, and provides further dose reduction to the sensitive organs in the anterior side of the patient, without increasing the dose for the posterior side. ODM proposes dose reduction by lowering the tube current for views that irradiate more radiosensitive tissues, such as anterior views for eye lens and breast tissue. However, the radiation dose and image quality effects of the ODM technique developed by GE Healthcare have not been quantified in the literature.

Specific Aim 1: Comparison of radiation dose in tissue locations with and without ODM

The thesis aimed to quantify radiation dose to tissues with and without ODM through experimental studies and Monte Carlo dose simulations. Dosimeters were placed at specific tissue locations to quantify dose in anthropomorphic head and chest phantoms. A clinical CT scanner equipped with ODM capability was used to perform phantom experiments under different TCM settings, keeping the other scanning parameters constant. Percent change in dose readings was then calculated to determine the effects of ODM on radiation dose. Monte Carlo simulation methods were validated against the experimental results using voxelized phantoms of the acquired axial slices. The study of ODM was extended to patients of varying sizes and anatomy by performing dose simulations on voxelized male and female phantoms from Duke's XCAT library

Specific Aim 2: Quantify noise in images acquired with and without ODM

The thesis also determined the effect of ODM on image quality by calculating noise standard deviation in the brain and heart regions of reconstructed images acquired through experimental studies. Ray tracing simulations were performed using GEANT4 toolkit for all voxelized XCAT phantoms, and an in-house filtered back-projection algorithm was used to reconstruct the images. Noise standard deviation was then calculated for the images acquired with and without ODM.

CHAPTER 2

Background

X-ray Radiation

X-rays are electromagnetic radiation that was discovered by Wilhelm Roentgen in 1895. Since then, X-rays have been used clinically all over the world for the study of bone fractures, kidney stones, lung cancer, tumors and other non-invasive diagnostic applications. The advent of computed tomography (CT) in 1971 was seen as a major advancement in diagnostic radiology where x-ray projections at multiple view angles could be used to acquire axial slices and 3D volumetric images of the body for studying precise location of tumors, cardiovascular diseases and a variety of other applications.

Formation of X-Rays

X-rays are emitted as a result of electron interaction with matter. Electrons travelling through matter interact with valence electrons resulting in electron transitions between atomic shells. Consequently, characteristic x-rays are emitted if the transition energy is greater than 100 eV. This type of x-ray radiation has specific energies depending on the binding energy difference of the atomic shells of the respective element. In some cases, the emitted radiation results in the ionization of nearby atom. The ejected electron in such interaction is referred to as an Auger electron. X-rays can also be formed as a result of interaction of electrons with nuclei of atoms. This causes the incident electron to deflect and lose some of its kinetic energy to the atom. Radiation

is emitted in a wide range of energies and is referred to as bremsstrahlung radiation. This type of x-ray radiation at various energy levels accounts for the majority of the radiation produced in clinical x-ray tubes. The probability of bremsstrahlung radiation increases as the square of atomic number of the material.

As x-rays travel through matter, they can either penetrate without interaction, or excite the electrons in matter through scatter or absorption. The type of x-ray interaction is dependent on the photon energy, and the properties of matter including atomic number, electron density and material density [3].

Interaction of X-Rays with Matter

Rayleigh Scattering

This type of scattering is also known as classical scattering, and occurs at very low photon energies, especially the energy range used in mammography. The traveling photon interacts with the whole atom and causes excitation of the electrons. However, the process only causes the orbiting electrons to oscillate, and therefore no ionization occurs. The emitted photon has the same wavelength and energy as the incident photon, but travels at a slightly different direction, as illustrated in Figure 1 below. The probability of Rayleigh scattering is inversely proportional to the square of the photon energy. Therefore, it counts for 5 to 10% of x-ray interactions in diagnostic imaging [3].

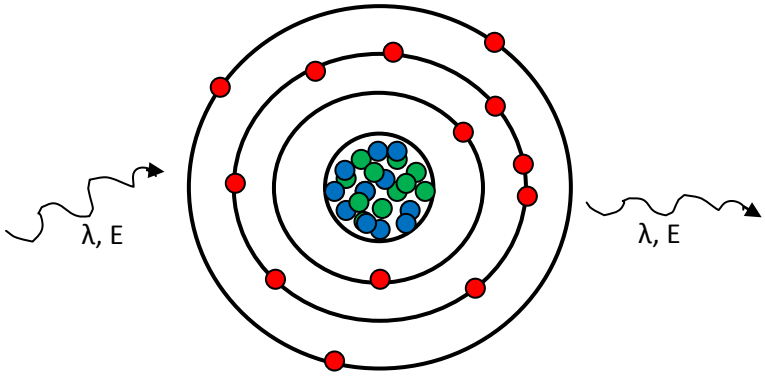

Figure 1: Rayleigh interaction of photons with matter, illustrated at atomic level

Compton Scattering

Compton or inelastic scattering is the most common type of x-ray interactions, accounting for more than 70% of interactions in medical imaging. The incident photon interacts with the valence electrons in the atoms, resulting in ionization of the atom. Therefore, for Compton scattering to occur, the energy of the incident photon must be greater than the binding energy of the ejected electron. The scattered photon loses some of its kinetic energy to the ejected electron, as shown in Figure 2 below. Since energy must be conserved, the energy of the incident photon is equal to the sum of the energy of scattered photon and the kinetic energy of the ejected electron.

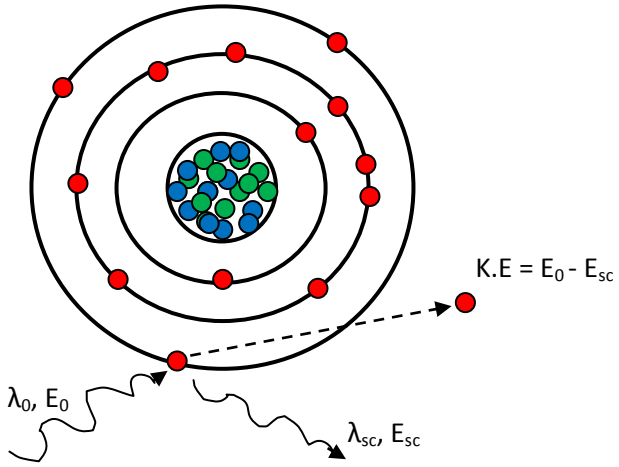

Figure 2: Diagrammatic representation of Compton Scattering at the atomic level

Given the incident photon energy, E_o and deflection angle, θ of the scattered photon, its energy can be calculated using equation 1 below [3].

$$E_{SC} = \frac{E_0}{1 + \frac{E_0}{511\ \text{keV}}(1 - \cos\theta)} \quad (1)$$

The probability of Compton scattering is fairly independent of atomic number of the material, but depends on the incident photon energy, electron density and mass density of the absorbing material. Most photons that interact with lower atomic mateials such as soft tissue, bone, etc. undergo Compton interactions at higher energies, and the Compton mass attenuation coefficient decreases with increasing photon energy. Hence, x-ray images acquired using high energy photons have less contrast among different tissues.

Photoelectric Absorption

In this type of interaction, the incoming photon interacts with an inner shell electron and transfers all of its energy to the electron, as shown in Figure 3 below. The kinetic energy of the ejected electron is equal to the difference between the energy of the incident photon and the binding energy of the electron. Electron cascade occurs as the outer shell electrons fill up the space of the ejected electrons. The auger electrons and characteristic photons released during the electron cascade possess very low energies and are absorbed quickly by the nearby atoms.

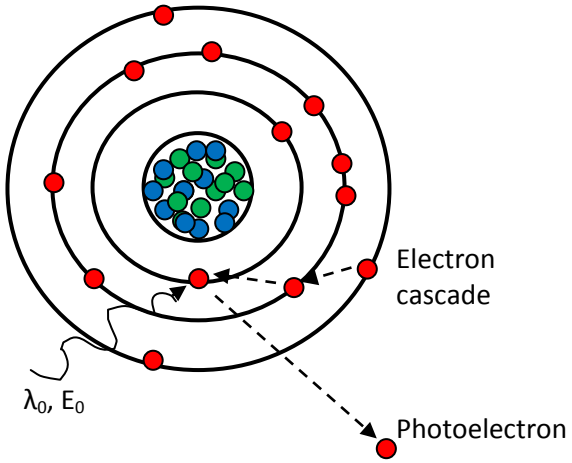

Figure 3: Photoelectric Absorption at the atomic level. The incident photon interacts with an inner shell electron causing it to be ejected. An electron cascade follows leading to the emission of characteristic x-rays.

Since the incident photon is completely absorbed by the atom, no scattering occurs, and therefore this type of interaction contributes positively towards the quality of image. The probability of photoelectric absorption is inversely proportional to the photon energy, and increases abruptly at photon energy very near to the binding energy of the

ejected electron. In addition, photoelectric absorption increases with increase in density and atomic number of the material.

X-ray Attenuation

As mentioned in the sections above, x-rays interact with matter and are either scattered or absorbed by the material. The amount of x-ray photons removed while passing through matter is referred to as x-ray attenuation. Linear attenuation coefficient is the fraction of x-rays removed from the x-ray beam per unit thickness of the material. It depends on the energy of the x-ray beam and the density of the material. For a mono-energetic x-ray beam, the number of photons exiting the material (N) can be calculated as a function of the total number of incident photons (N_o), material thickness (x) and the linear attenuation coefficient (μ), using the Lambert-Beer law as shown in equation 2 below.

$$N = N_O e^{-\mu x} \quad (2)$$

The linear attenuation coefficient is a function of photon energy. Therefore, the number of photons exiting a number of materials for a polyenergetic x-ray spectrum can be calculated using equation 3 below:

$$N = \int_{E_1}^{E_2} N_O(E)\, e^{-\int \mu(x,E)dx}\, dE \quad (3)$$

Radiation Dose

Radiation dose for various applications is measured in units specified by the International Commission on Radiation Units and Measurements (ICRU) and the International Commission on Radiological Protection (ICRP). Absorbed radiation dose is the amount of ionization energy transferred per unit mass of the material. It is independent on the type of ionization energy used, and is usually measured in units of gray (Gy), where 1 Gy = 1 J/kg.

Equivalent Dose versus Effective Dose

Although absorbed dose provides information about the quantity of dose imparted to the material, it does not take into account the type of ionization radiation used. Since the effect of radiation on biological tissues depends on the type of radiation, another metric called as equivalent dose was adopted by the ICRP that provided a weighting factor for different radiation types. For x-ray and gamma radiation, the weighting factor is 1, and therefore the absorbed dose is equal to the equivalent dose in the case of these radiation types [3]. Neutrons and alpha particles have radiation weighting factors ranging from 2.5 - 20, thereby having a greater detrimental effect on the tissues than x-rays or gamma rays. In addition to the type of ionizing radiation used, the levels of harmful effects caused due to the radiation depend on the biological tissue exposed.

Effective dose is another metric for dose measurement that takes into account the tissue weighting factors assigned by the ICRP, according to which the breast and lung tissue together add up to approximately 25% of the total detriment from stochastic radiation effects [3]. Effective dose and equivalent dose are both measured in units of

Sievert (Sv), where 1 Sv = 1 J/kg. While equivalent dose only takes into account the type of radiation used, effective dose accounts for both the type of radiation and the type of biological tissue exposed.

CT Dosimetry and Organ Dose

The amount of dose delivered to the patient during a CT scan is usually measured using a standardized index called computed tomography dose index (CTDI). $CTDI_{100}$ is typically measured using dosimeters in a 100 mm long chamber, contained inside a 16 cm or 32 cm polymethyl methacrylate (PMMA) phantom. Five dosimeters are placed, one in the center and and four in the periphery of the PMMA phantom, and the weighted CTDI is calculated using equation 4 below.

$$CTDI_{weighted} = \frac{1}{3} CTDI_{100,center} + \frac{2}{3} CTDI_{100,periphery} \quad (4)$$

The 16 cm PMMA phantom represents an adult head or a pediatric torso phantom, whereas the 32 cm phantom represents an adult torso. CTDI depends on the scanning parameters including helical pitch, tube current, exposure time, and tube voltage. Estimated CTDI information is readily available even before the scan is performed on most clinical scanners as soon as the above mentioned parameters are defined by the user. Although a standardized measure, CTDI has various limitations including the lack of dose information for non-cylindrical and non-homogenous bodies such as human body [11]. In addition, the dosimeters in CTDI measure dose to the air, and therefore the values cannot be used for specific tissues in the body. Lastly, the CTDI values are independent of patient dimensions and therefore do not accurately represent dose for

differently sized patients. However, conversion factors are available through the American Association of Physicists in Medicine (AAPM) to calculate size specific dose estimates (SSDE). In order to overcome the shortcomings of CTDI, specific organ dose measurements are required to estimate radiation dose to human patients. Such measurements are usually performed using Monte Carlo dose simulations, explained in the next section.

Monte Carlo Dose Computation

Monte Carlo computation method is a statistical tool based on the laws of probability that has become increasingly popular in various medical physics applications due to the stochastic nature of radiation emission and transport, as well as availability of parallel computing systems. This study used GEANT4 (GEometry ANd Tracking) software toolkit that incorporates Monte Carlo methods to simulate the interaction of particles through matter [12]. The system takes into account Rayleigh, Compton and other interactions of photons with matter using low energy physics models described through the GEANT4 Livermore Library. The toolkit allows stochastic modeling and tracking of particles through complex geometries and estimation of energy deposited at specific locations through simulation of a number of photon particles specified by the user. The statistical reliability of Monte Carlo methods depends on the number of particles simulated to estimate the physical quantity. Therefore, it is essential to determine an appropriate number of photons simulated in order to get a low standard deviation between dose estimation trials.

Effects of Radiation Exposure

Although medical imaging modalities, including x-ray radiography and CT hold an important place in non-invasive diagnosis of diseases, the effects of radiation exposure due to these modalities have become a great concern to the medical professionals and patients in the recent years. Although CT scans contribute for about 15% of all the radiological procedures performed annually, CT radiation dose accounts for 75% of the total administered radiation dose [11].

Radiation Risk to Patients

. An x-ray dose of more than 10 mSv can increase the possibility of a fatal cancer by 0.05% [4]. This percentage may become increasingly significant especially in a large population undergoing radiation exposure due to CT scans. Since the effective dose due to CT scans is higher than that administered in a planar x-ray scan, CT procedures are responsible for much higher health risks to patients. For example, the effective dose due to a single CT head scan is approximately equal to the effective dose due to 100 chest x-ray scans. Similarly, a CT abdomen scan is capable of delivering an effective dose that is about 400 times higher than that of a single chest x-ray. Two types of health risks are associated with ionizing radiation exposure - deterministic and stochastic. Deterministic radiation effects are characterized by a dose threshold and severity of effect. For example, cateractogenesis is a deterministic radiation effect in the eye lens that initially had a dose threshold of 1.9 Gy, but has recently been reduced to 0.5 Gy [13].

Stochastic radiation effects include carcinogenesis and mutations in the DNA. The probability of stochastic radiation effects is directly proportional to the amount of

dose administered. However, the severity of the effect is unrelated to the amount of dose. It is estimated by the National Cancer Institute (NCI) that CT scans performed in the year 2007 alone will be responsible for causing 29,000 excess cancer cases during the lifetime of the patients exposed [14]. A study conducted on an anthropomorphic female phantom using a multi-detector CT scanner used estimated organ dose to calculate the lifetime attributable risk (LAR) of breast and lung cancer incidence in male and female patients of ages between 15 and 55 years [15]. The radiation risks calculated in the study were based on results of the BEIR VII report, which represents cancer incidence in Japanese atomic bomb survivors. The study estimates the LAR of breast cancer incidence in females between the ages of 15 and 55 to be between 46 and 503 for a particular CT angiography protocol [15]. Although the lifetime excess relative risk of breast cancer is low (ranging from 0.2 to 0.4) for women aged 55 years and older, the risk is significantly higher for girls and young women especially those undergoing a single examination of ECG-gated CT angiography protocol. The LAR of breast cancer increases by at least 6 times for women 25 years and younger for all CT protocols. It should be noted that these results are only representative of a single examination of the given CT protocols, and the relative risk would increase additively for subsequent scans.

CT Physics

CT has been widely used as a diagnostic imaging modality to acquire planar and volumetric 3D images using x-ray projections at multiple view angles. The basic components involved in the design of a clinical CT system include the x-ray source, collimator, beam filters and detector plate. The above components constitute the gantry that rotates around the patient to acquire 2D x-ray images. These projections are then reconstructed using computational algorithms to acquire the desired images. The sections below provide a brief description of the system design and reconstruction algorithms used in the current CT systems.

System Design

Gantry Geometry

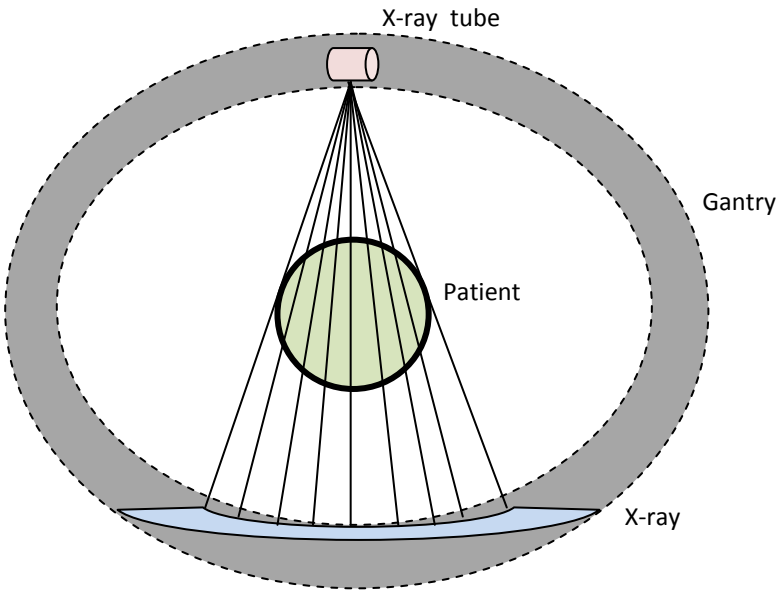

Figure 4: Diagrammatic representation of CT gantry geometry

Figure 4 above illustrates a block diagram of the gantry system, which includes an x-ray source and detector. Current clinical systems are able to achieve rotation times of less than 0.5 seconds per 360 degree rotation. In order to acquire about 1000 or more projections at this rotation speed, fast and reliable data transfer between the rotating gantry and stationary CT components is made possible with the slip ring technology [16]. The slip rings are able to eliminate cable connections between components by passing electrical power using sliding metallic brushes. Therefore, data from the detector channels is transferred without any inter-scan delays [17].

X-ray source, filtration and collimation

X-rays used in CT systems are generated in an x-ray tube that consists of an anode and cathode, powered by a high voltage generator. The negatively charged cathode serves as the source of high speed electrons that bombard against the positive anode (typically made of tungsten) to generate x-rays. The energy and number of generated x-rays depend on the potential difference (between the anode and cathode) and filament current, respectively [16]. During this process, less than 1% of the kinetic energy of the electrons is converted to x-rays and the rest is dissipated as heat, which may lead to over-heating of the anode. In order to overcome this limitation, several techniques are applied to reduce x-ray tube heating such as tilting the anode angle to increase the size of the actual focal area, having a rotating anode to distribute the heat evenly to a large area and employment of computational tube cooling algorithms [16].

Interaction of electrons with the anode produces characteristic x-rays having specific energies as well as Bremsstrahlung x-rays having a wide range of energies. The characteristic x-ray emissions occur through electron cascade during excitation or ionization of electrons in the target material, and the energy of x-rays produced is the difference between the atomic energy levels. On the other hand, Bremsstrahlung x-rays are produced when the travelling electron is close to the nucleus of the target atom. It gets deflected and loses some of its kinetic energy to produce radiation.

The x-rays exiting the tube consist of a wide energy range as described above. The soft x-rays (lower energy photons) are usually unable to penetrate through the patient body, thereby increasing the absorbed patient dose but not contributing to the x-ray image. Hence, the x-ray beam is filtered before it interacts with the patient to reduce radiation dose. In addition, collimators are also placed between the x-ray source and patient and are used in CT systems to reduce the width of the x-ray beam. The beam width can be adjusted using these collimators to determine the slice thickness in single slice scanners. Collimators limit the radiation exposure area and therefore help to reduce unnecessary dose to patients.

Bowtie Filter

In addition to the beam-shaping filter discussed above, a bowtie-shapted filter is also used in most clinical CT systems to adjust the intensity of x-rays with the goal to equalize the x-ray flux to the patient along the in-plane detector-direction [3]. It also removes low-energy photons from the x-ray beam to further help in dose reduction. The filter width is thicker at the periphery of the patient body and narrows towards the center.

The filter shape also helps in improving the image quality by reducing the x-ray scatter-to-primary ratio [18, 19]. Aluminum and polymethyl metacrylate (PMMA) are typically used as materials for the bowtie filter, but specific composition is proprietary information for scanner manufacturers [20].

Multi-detector Volume CT

Single-slice CT systems consist of a single row of x-ray detectors and have several limitations such as long scan times and poor x-ray tube utilization due to thin collimation. These shortcomings led to the development of multi-slice CT systems where multiple rows of detectors are added in the slice direction. This allows to increase the width of the beam for better tube efficiency and hence the slice thickness can be adjusted as integer multiples of the size of the detector pixel in the slice direction. Since the tube collimation is opened up in the slice direction, the beam shape changes from a fan-beam to a cone-beam in multi-detector CT. However, it is important to note that too many detector rows in the slice direction along with a wider cone beam may lead to cone-beam artifacts. These artifacts result because the projection planes (except that created by the central row of detector) are not exactly parallel to the axial plane [21]. These artifacts can either be corrected using computational reconstruction algorithms, or reduced by limiting the width of the cone beam.

Image Reconstruction

The 2D x-ray projections acquired in a complete 360 degree rotation can be reconstructed into axial slices using two commonly used reconstruction algorithms -

filtered backprojection and iterative reconstruction. If a single point in a projection image is plotted against all view angles, a sinusoidal curve is obtained. Similarly, if the single point is replaced by one row of points in the x-direction, a number of overlapping sinusoidal curves are obtained, as shown in Figure 5 below. This collection of points over all projection angles is referred to as a sinogram, and is a useful debugging tool to diagnose defects in the CT system [16].

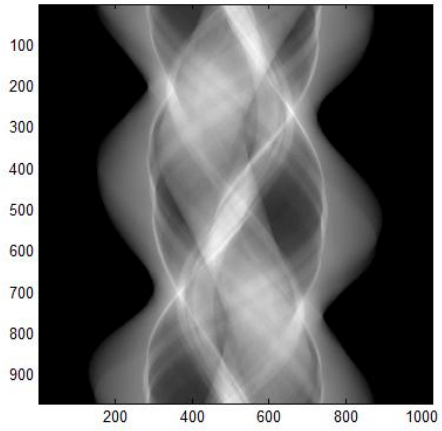

Figure 5: Sinogram data representing a single row of detector for all projection angles

In filtered backprojection reconstruction algorithm, the projection values at all angles are smeared back to form the CT image [3]. However, in order to reduce the blurring effect in the reconstructed images, the projection data is convolved with a deconvolution kernel before backprojection. To speed up the computation process, the Fourier transform of the projection data is multiplied with the Fourier transform of the convolution kernel (also called as the ramp filter), and the inverse Fourier transform of the resulting data is the CT image. The basic idea behind iterative reconstruction algorithm is to closely match the reconstructed image with the measured data. An initial

guess image is used to calculate the predicted projection data. The difference between the predicted and actual projection data is the error matrix. The guess image is corrected based on this matrix, and the process is repeated at all projection angles until the error is reduced to a pre-determined error matrix. Although filtered backprojection has been the most commonly used algorithm for CT systems, iterative reconstruction method is now gaining popularity due to availability of better computing resources. Images acquired through the iterative technique have demonstrated to have lower image noise than filtered backprojected images [22].

CT Dose Reduction Techniques

In order to minimize the health risks involved with radiation exposure in CT scans, several dose reduction techniques have been proposed and are employed in commercial CT systems. Some of the methods include filtration to remove low-energy x-rays (as discussed in sections above), tube current modulation, and breast shields.

Breast Shields

Breast shields refer to bismuth latex sheets that are used to cover the breasts during CT scans [23]. These reusable sheets are also sometimes used for other anterior organs including the eye lens and thyroid. They help in reducing radiation dose to anterior organs by absorbing some of the x-ray radiation before it hits the patient. However, the AAPM and other studies suggest that breast shields cause image artifacts such as beam hardening and streak effects, and therefore discourage the use of these shields if other dose reduction techniques are available [23, 24, 25, 40]. These studies

suggest tube current modulation that may offer equivalent dose reduction as breast shields without degrading the image quality.

Tube Current Modulation

Tube current (measured in milliamperes or mA) refers to the amount of current flowing between the anode and cathode in the x-ray tube. The number of photons exiting the x-ray tube is directly proportional to the tube current. Therefore, amount of radiation dose to the patient can be reduced by limiting the current flow in the x-ray tube. Tube current modulation (TCM) is a dose reduction technique that adjusts the tube current in the angular and/or slice directions based on patient attenuation, as illustrated in Figure 6 below [26].

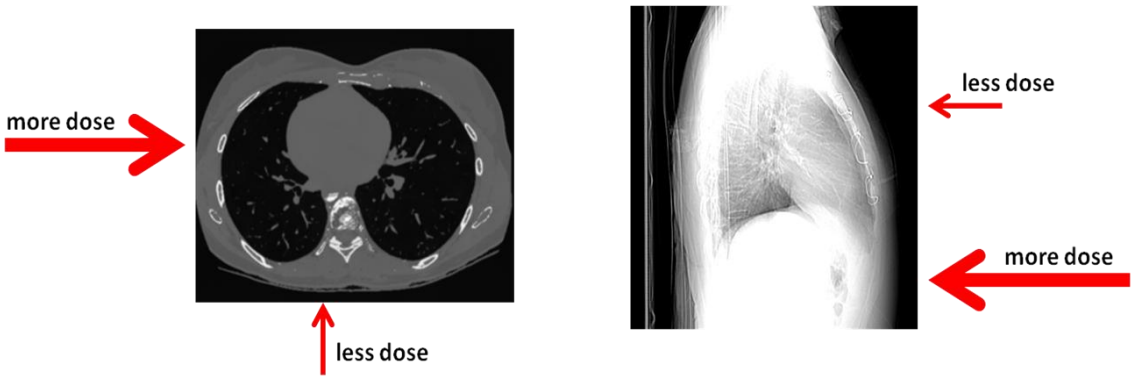

Figure 6: Axial slice and lateral scout showing relative dose after the application of tube current modulation in angular and slice directions, respectively

An anteroposterior (AP), posteroanterior (PA) or lateral radiograph is performed before the actual scan to determine patient size and shape using attenuation values. The tube current in the x, y and z directions are then calculated by the CT system based on the

radiograph and other CT parameters including the noise index, scan time, slice thickness and range of tube current [27]. Typically, an AP scout is used to generate the mA table since it computes the lowest dose as compared to that generated by PA or lateral scout [27]. Previous works on three-dimensional TCM (angular and slice direction tube current modulation) that measured dose changes to radiosensitive organs have demonstrated a net dose reduction by up to 64% to the breast tissue and 56% in the lung tissue as compared to the fixed mAs (tube current-scan time product) protocol [30, 31]. Smaller patients received a greater dose reduction in the breast and lung tissue with TCM as compared to the larger patients. In 9 out of the 30 patient models studied, TCM resulted in a net increase in dose to the breast and lung tissues by up to 41% and 33%, respectively [30].

Other studies have discussed organ-based TCM that implements a modification to the TCM method cited above by further reducing tube current at the anterior views of the patient and increasing it for posterior views [38, 39]. The total tube current is kept constant as for the reference protocol per 360° rotation. Therefore, the image quality measured using noise standard deviation in the reconstructed images is comparable for both reference and organ-based TCM protocols. However, in this case, increased tube current at the posterior views may lead to an increased absorbed dose for the spine, lung and other tissues [30, 38]. Since both lung and breast have equal tissue weighting factors of 0.12 [3], an increase in the dose to lung or other radiosensitive tissues using organ-based TCM may lead to a net increase in the effective dose to the patient. A study estimated the breast dose reduction by 5 - 32% in chest CT scans, but an increase in the posterior skin dose by 11 - 20% using this protocol [38].

GE Medical Systems employs a software-based TCM technique called AutomA in their clinical scanners to modulate the tube current in the z-axis (slice direction) based on a single patient scout [27]. The absolute tube current values are a function of patient attenuation and scan parameters such as noise index, beam collimation, slice thickness and tube voltage. AutomA technique uses a fixed tube current for each gantry rotation. A 3D modulation technique called SmartmA is also available on these scanners as an additional feature to AutomA for both angular (x- and y-axis) and z-axis modulation. In addition to SmartmA, GE proposes a new organ-based modulation technique (ODM) that is comparable to the organ-based TCM method described above, but differs in that it does not increase radiation dose for the posterior views. Therefore, the total tube current per 360° rotation is reduced as compared to the reference protocol. The sections below describe the methods and results to quantify the effects of GE's ODM implementation on radiation dose and image quality.

CHAPTER 3

Materials and Methods

Although several studies have shown that significant dose reduction can be achieved using the TCM technique, this study focuses on a new ODM implementation that provides additional dose reduction by decreasing the tube current for the anterior views in order to reduce the dose to radiosensitive organs, without increasing the dose for the posterior views. The change in dose and noise for ODM relative to AutomA and SmartmA modulation settings was first measured experimentally for an anthropomorphic phantom. A simulation workflow was developed with Monte Carlo simulations that estimated dose, ray-tracing simulations that generated images, and a software tool that generated AutomA, SmartmA, and ODM tube current profiles to emulate the scanner functionality. The simulation workflow was first validated with the experimental data, and then used to study the effects of ODM for a voxelized phantom library. The sections below describe the specific experimental and simulation methods. .

Experimental Methods

Axial CT scans at 120 kV were performed on anthropomorphic head and chest phantoms (Rando Alderson Research Laboratories, Stanford, CA) on an ODM-equipped scanner (Optima CT660, GE Healthcare, Chalfont St Giles, England). ODM has different pre-set modulation settings for chest and head exams. Thirteen MOSFET dosimeters (mobile MOSFET Dosimetry System, Best Medical, Ottawa, Canada) were placed at tissue locations in the breast, lung, heart, spine, eye lens and brain regions to

quantify radiation dose as illustrated in Figure 7. For the head phantom, a total of five dosimeters were used - two in the eye region (one for each eye), two in the central brain region and one in the back region of the head. Eight dosimeters were placed in the chest phantom - four in the breasts (two each for left and right breasts in both inferior and superior regions), two in the lungs (one each for left and right lung), one in the heart and one in the spine.

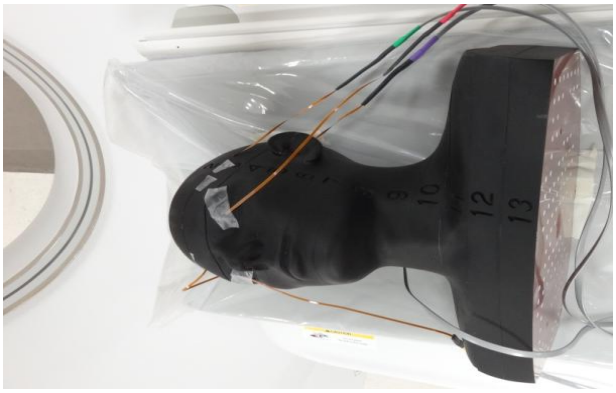

Figure 7: Anthropomorphic head phantom with dosimeters placed in the eye lens and brain regions

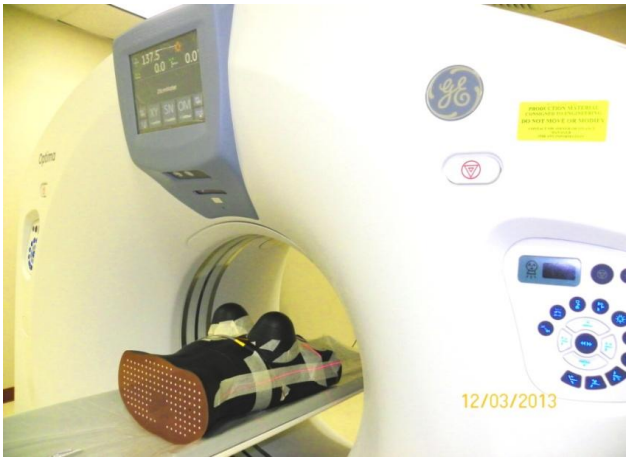

Figure 8: CT scan of an anthropomorphic chest phantom with dosimeters in breast, lung, heart and spine regions

For the head phantom, five scans were performed with SmartmA and ODM, with all other scan parameters held constant. Each scan was performed using seven axial rotations, gantry rotation speed of 2 seconds, 0.5 cm slice thickness and 14 cm total volume thickness. The noise index parameter was held constant at 2.8 and a total of 1,968 projection images (0.183 degrees/view) were acquired for each axial rotation. The chest phantom was scanned at AutomA, SmartmA and ODM settings, with six axial rotations, gantry speed of 1 second, 0.25 cm slice thickness and 24 cm total volume thickness. The noise index parameter was set to be 7.0 and 984 projections (0.366 degrees/view) were acquired in one axial rotation. AutomA scans were not performed for the head phantoms. Since the head is mostly circular in shape, it is expected that AutomA and SmartmA would provide similar results.

Percent change in dose was calculated with respect to non-ODM measurements for all dosimeters. To assess the effect of ODM on image quality, noise standard deviation was calculated in 15 x 15 pixel regions of interest (ROIs) in the brain and chest regions of all reconstructed images.

Simulation Methods

Modeling the CT system in GEANT4

A CT system was modeled in GEANT4 with a 120 kVp x-ray source, source-to-detector distance of 95 cm and source-to-isocenter distance of 54 cm. The detector was modeled to be of the same size as the extent of the beam collimation of 105.0 cm x 3.5 cm for the head scans and 105.0 cm x 7.0 cm for the chest scans. Multiple axial rotations were performed to scan the entire phantom. A beam-shaping bowtie filter was

also modeled using the information provided in literature [20]. The Monte Carlo software simulated and tracked the transport of polyenergetic photons through voxelized phantom objects. The number of photons tracked for each view angle and scan rotation varied depending on the study, as will be described in more detail. The output of the Monte Carlo simulations was the absorbed radiation dose in eV at each voxel location of the phantom at each view angle and gantry z-location. The percent change in dose for ODM was calculated for all segmented tissues with respect to AutomA and SmartmA using equations 5 and 6 below.

$$Percent\ change\ in\ dose\ wrt\ AutomA = \left(\frac{Dose_{ODM} - Dose_{AutomA}}{Dose_{AutomA}}\right) x\ 100 \quad (5)$$

$$Percent\ change\ in\ dose\ wrt\ SmartmA = \left(\frac{Dose_{ODM} - Dose_{SmartmA}}{Dose_{SmartmA}}\right) x\ 100 \quad (6)$$

Ray tracing simulations were also implemented to calculate the distance travelled through each material for each ray connecting the source to the detector at all view angles and gantry z-locations. The resolution for the detector pixels was 0.09765 cm x 0.09765 cm. Based on this distance, the number of photons, N reaching each detector pixel was calculated using Beer Lambert's law described in equation 3 in Chapter 2. The total number of incident photons, N_0 for each projection angle and scan rotation was directly proportional to the tube current value for that angle and rotation, as will be described in the following section. Poisson noise was added to the detected number of counts. Lastly, the number of photons at each detector pixel was log normalized using equation 7 below:

$$-\ln\frac{N}{N_0} = \int \mu(x)dx \quad (7)$$

Determination of tube current for AutomA, SmartmA, and ODM settings

A standalone version of GE's proprietary tube-current modulation algorithm was implemented in MATLAB to emulate the generation of tube current profiles for the different TCM settings. The ray-tracing simulation software generated an AP scout for all voxelized phantoms. This scout was input to the standalone software to determine the tube current for each view angle and gantry z-location for the three investigated TCM settings: AutomA, SmartmA and ODM. Other scan parameters required as input for the tube current algorithm such as slice thickness, collimation and tube voltage were kept constant at 0.325 cm, 2.0 cm and 120 kV for the head phantoms, and 0.1 cm, 4.0 cm and 120 kV for the chest phantoms, respectively. Although the noise index (NI) which is also used as an input for the tube-current algorithm could vary depending on phantom size, it was held constant across the three investigated TCM settings and across all phantoms. Since NI only contributes as a scaling factor in determining the tube current, it does not affect the relative ODM tube current with respect to AutomA and SmartmA settings.

Figure 9 displays a simulated AP chest scout and Figure 10 shows a plot of the tube current profile output by the GE algorithm for one scan position at AutomA, SmartmA and ODM settings. As can be seen in Figure 10, the AutomA tube current was constant across all view angles, although it varied with the z-location of the gantry. SmartmA varied sinusoidally in the angular direction, with the maximum tube current in the lateral views (90° and 270°), and minimum tube current in the AP and PA views (0° and 180°). For this phantom and gantry position, SmartmA used 96.2% of the photons of the AutomA scan. The ODM tube current setting is a modification to the SmartmA where the tube current is further reduced for the anterior views. The percent reduction in tube

current and the fan angle is dependent on the scan type and gantry rotation time. Routine head scans conducted with gantry rotation time of 2.0 seconds experience tube current reduction of 30% between -55° and 53° view angles (where 0° refers to AP position). For chest scans, the tube current is reduced by 40% between -91° and 89° view angles. For this phantom, ODM used 76.8% of the photons of the AutomA scan.

The tube current profiles generated by the GE algorithm, as plotted in Figure 10, determined the number of photons, N_o, simulated for each view angle and gantry z-location. For Monte Carlo dose simulations, N_0 was calculated as a constant integer multiple of the tube current profiles for AutomA, SmartmA and ODM. Since dose simulations were only used to estimate relative dose for ODM with respect to AutomA and SmartmA, the range of N_0 was kept high enough to obtain statistically reliable radiation dose values with very low standard deviation between trials. A similar strategy was used to determine N_0 for ray tracing simulations, where the normalized tube current profiles were multiplied by a constant integer, 7.4E5. The range of N_0 was selected to obtain a realistic range of noise standard deviation in the reconstructed images (~7 to 20 HU).

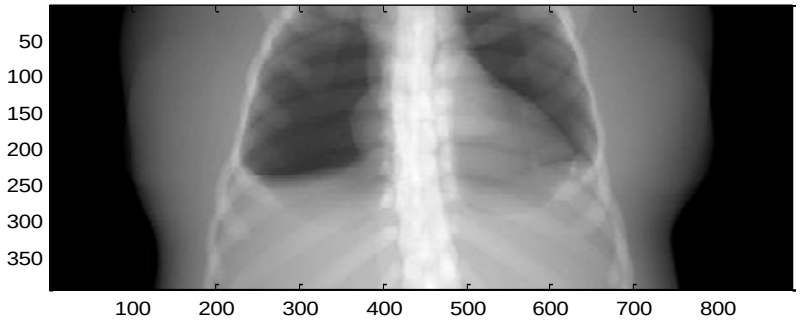

Figure 9: AP chest scout obtained through ray tracing simulation in GEANT4

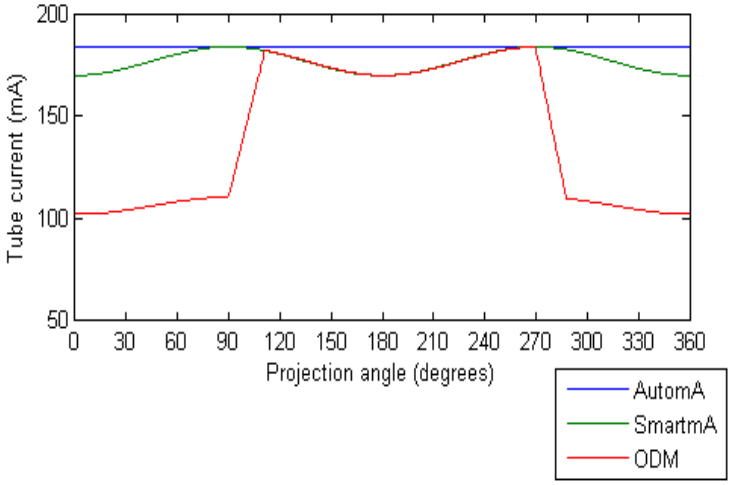

Figure 10: Tube current at each projection angle for one scan rotation of a chest phantom

Image Reconstruction

The log normalized data from the ray tracing simulations were reconstructed into axial slices using an in-house filtered back-projection algorithm with a volume resolution of 0.05 x 0.05 x 0.05 cm^3 for both head and chest images. The pixel values of the reconstructed images were converted from attenuation, μ to Hounsfield units (HU) using equation 8 below, where attenuation coefficient of water (μ_{water}) is 0.2.

$$houns = 1000 \frac{(\mu - \mu_{water})}{\mu_{water}} \quad (8)$$

To assess the effect of ODM on image quality, relative noise and percent change in noise were calculated in the reconstructed images with respect to AutomA and SmartmA using equations 9 through 12 below.

$$Relative\ Noise\ wrt\ AutomA = \frac{Noise_{ODM}}{Noise_{AutomA}} \quad (9)$$

$$Relative\ Noise\ wrt\ SmartmA = \frac{Noise_{ODM}}{Noise_{SmartmA}} \quad (10)$$

$$Percent\ change\ in\ noise\ wrt\ AutomA = \left(\frac{Noise_{ODM} - Noise_{AutomA}}{Noise_{AutomA}}\right) x\ 100 \quad (11)$$

$$Percent\ change\ in\ noise\ wrt\ SmartmA = \left(\frac{Noise_{ODM} - Noise_{SmartmA}}{Noise_{SmartmA}}\right) x\ 100 \quad (12)$$

Validation of Simulation Methods with Experimental Data

The simulation workflow was validated by performing simulations on a voxelized version of the experimental anthropomorphic phantoms. To create the phantom, the volume of experimental axial head and chest images were segmented into four materials - air (< -200 HU), water (-200 to 5 HU) , soft tissue (5 to 280 HU) and bone (> 280 HU). The x-ray mass attenuation values for the segmented materials were obtained from the National Institute of Standards and Technology (NIST) for the energy range between 20 and 120 kV [32]. Scout images of these voxelized phantoms in the AP direction were simulated using the ray tracing software. Using these scouts and the proprietary GE algorithm, tube current profiles were generated for these phantoms for AutomA, SmartmA and ODM settings. The tube current profiles generated by the software workflow for the voxelized phantom were compared with profiles generated by the scanner for the experimental phantom.

The dosimeter locations in the experimental images were segmented in the voxelized phantoms. The absorbed dose to the dosimeter locations was estimated using the Monte Carlo simulation software. The percent change in dose for ODM with respect to AutomA and SmartmA was compared for both experimental and simulated results. Ray tracing simulations were also performed for 984 view angles (0.366 degrees/view) on the voxelized phantom for the AutomA, SmartmA, and ODM settings, followed by

filtered backprojection reconstruction. Noise standard deviation was calculated in three 15 x15 ROIs in each reconstructed simulated image. Relative noise with respect to AutomA and SmartmA was then compared for both experimental and simulated images.

Simulation Studies for Varying Patient Anatomies

In order to study the effects of ODM on radiation dose and image quality for patients of varying sizes and anatomy, simulations were conducted on a set of male and female voxelized phantoms, as described below.

Voxelized Phantoms

Voxelized, full-body female and male adult phantoms were acquired from Duke's extended cardiac-torso (XCAT) phantom library [33]. These phantoms were created at Duke University by segmenting CT image data into tissue types. For the purpose of this study, the head phantoms were segmented into eight materials - air, water, brain, blood, cartilage, bone, muscle and eye lens, while the chest phantoms were segmented into nine materials - air, lung, soft tissue, muscle, glandular breast, blood, bone, water and cartilage. The x-ray mass attenuation values for the segmented materials were obtained from NIST for the energy range between 20 and 120 kV [32]. This study used a total of 28 head (15 male and 13 female) and 10 chest (all female) phantoms from the XCAT library. Axial slices of the head phantoms were generated from the XCAT library with slice thickness of 3.125 mm and axial resolution of 0.825 mm/pixel. Similarly, axial slices of the chest phantoms had 1.0 mm slice thickness and 1.0 mm axial resolution.

Scout images of these phantoms were obtained using ray tracing simulations to generate tube current profiles for AutomA, SmartmA, and ODM scan settings. Monte Carlo dose simulations in GEANT4 were performed for all head and chest phantoms and percent change in dose with respect to AutomA and SmartmA was calculated. Ray tracing simulations were performed to compare the noise standard deviation of AutomA, SmartmA, and ODM settings, with 968 view angles at 0.372 degrees/view. Pixel standard deviation was calculated in brain and chest regions of the reconstructed images at all tube current settings - AutomA, SmartmA and ODM. For each reconstructed image, noise standard deviation was calculated in three, 15 by 15 pixel regions of interest (ROI).

CHAPTER 4

Results

Experimental Studies Using Anthropomorphic Phantom and Clinical Scanner

ODM reduced the dose at all dosimeter locations, with dose changes of -31.3% in the breast, -20.7% in the lung, -24.4% in the heart, -5.9% in the spine, -18.9% in the eye and -10.1% in the brain, with respect to SmartmA as shown in Figure 11 below. The percent change in average dose for the chest scans with respect to AutomA was -37.7%, -29.8%, -35.3% and -25.0% in the breast, lung, heart and spine, respectively. Multiple dosimeters were placed in the breast, lung, eye and brain regions, and therefore percent change in dose values were averaged to represent the absorbed dose for these tissues.

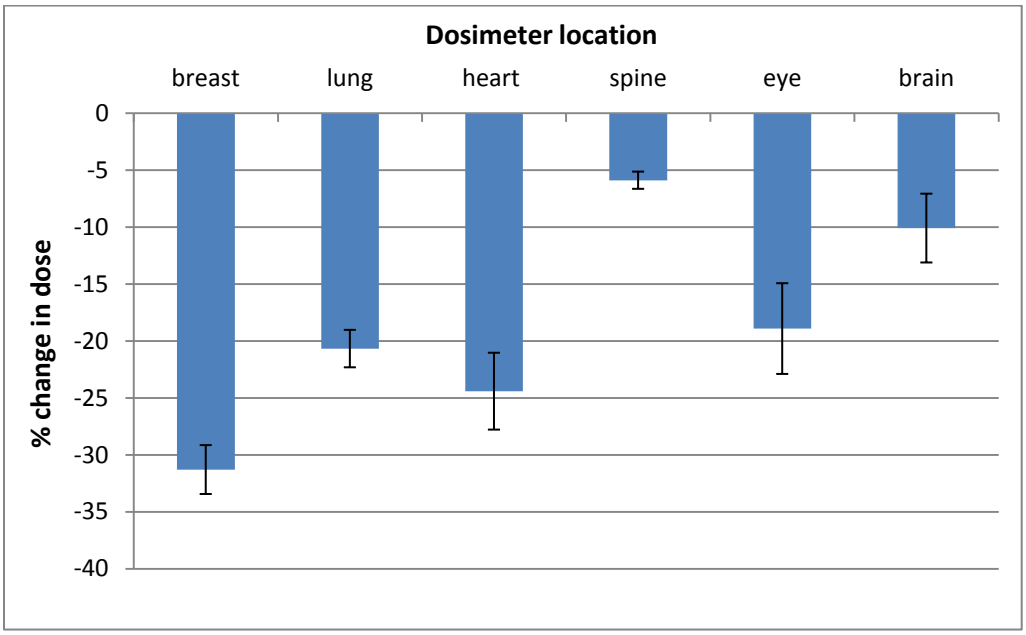

Figure 11: Percent change in dose with respect to SmartmA measured using MOSFET dosimeters during experimental studies

ODM increased noise standard deviation by 8.0% and 4.1% with respect to SmartmA in head and chest scans respectively. The percent change in noise with respect to AutomA for chest scans was 10.3%.

Validation of Simulation Methods Ssing Experimental Results

Figure 12 below plots validation results comparing the tube current profiles generated by the simulation workflow with those generated by the scanner for the experimental phantom. The results show close agreement between simulated and experimental mA profiles within 2% error for tube current values in both lateral and AP directions.

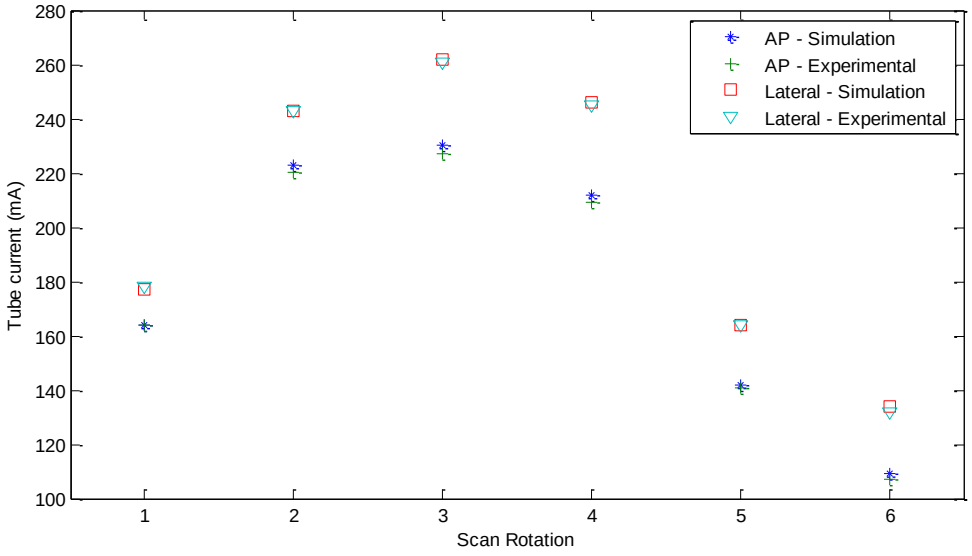

Figure 12: Tube current values in the AP and lateral directions for an experimental and simulated chest scout image

Figures 13 and 14 present the results of the simulation validation study, where the percent change in dose for ODM is compared for the experimental and simulation results with respect to AutomA and SmartmA scan settings. It should be noted that AutomA scans were not conducted for the head phantom during the experimental study. Because the head region has more circular shape, the AutomA results are expected to be similar to the SmartmA results. Therefore, absorbed dose for the eye lens and brain tissue are only available for the SmartmA setting.

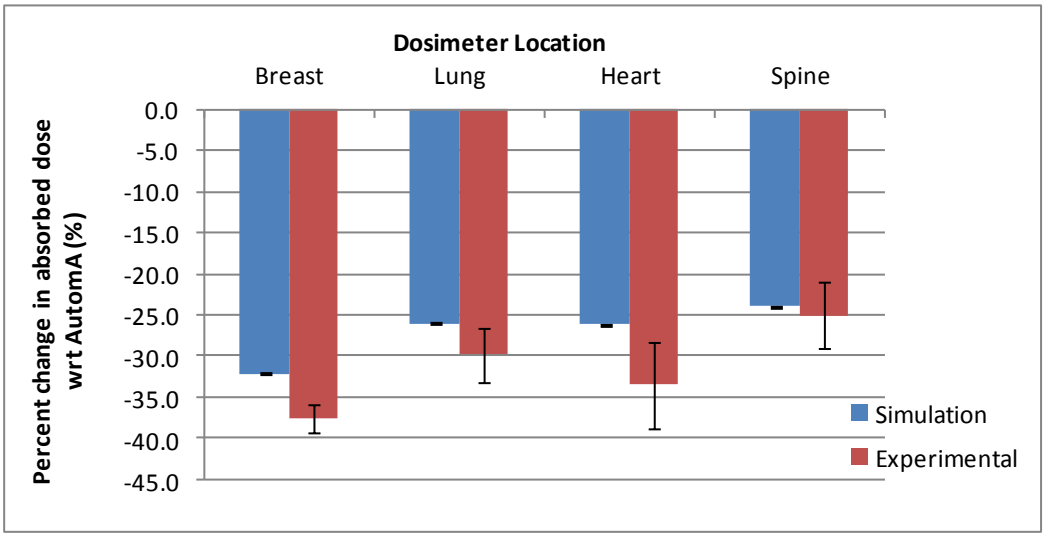

Figure 13: Comparison of experimental and simulation dose results with respect to AutomA for chest scans

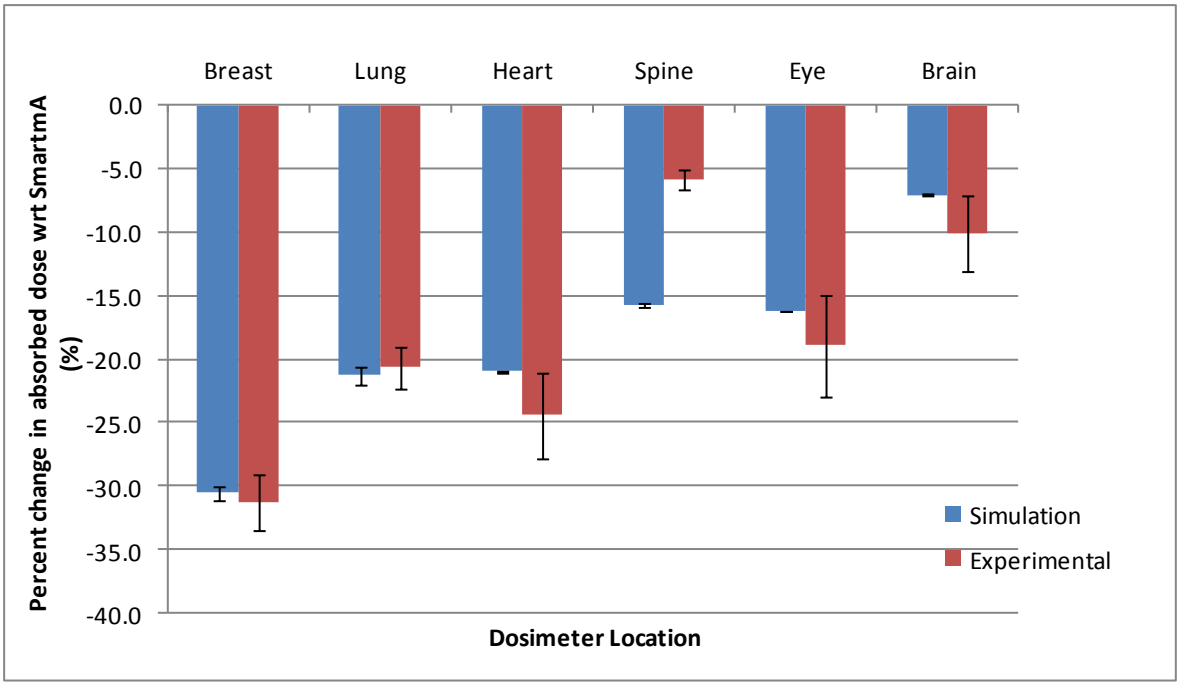

Figure 14: Comparison of experimental and simulation dose results with respect to SmartmA for head and chest scans

Percent change in average dose values calculated using Monte Carlo simulations are within 3.4% to the experimental data at all dosimeter locations except at the spine region in the SmartmA scan. Simulations estimated a lower change in dose compared to the experiments for all cases except the spine and lung tissue. This discrepancy may be due to differences in the simulated material properties compared to the true phantom materials. The discrepancy in the spine may be due to placement of the dosimeter, as dosimeters are sensitive to angular position. Another potential explanation of the discrepancy in the spine measurement is that the beam intensity has been found to vary with position relative to the table [34], and the spine dosimeter was placed closest to the table.

Table 1 lists the percent difference in image noise for experimental and simulated axial images acquired with and without ODM. Noise standard deviation increased by

8.0% and 4.1% with respect to SmartmA in the experimental head and chest images, respectively. A similar trend was observed in simulated images with an increase in noise by 6.5% in the head and 6.1% in the chest regions with respect to SmartmA.

Table 1: Validation of simulation methods for image quality with experimental results using noise standard deviation

Scan Protocol	Percent change in noise standard deviation for ODM with respect to …			
	AutomA		SmartmA	
	Experimental	Simulated	Experimental	Simulated
HEAD	N/A	N/A	7.99	6.46
CHEST	7.80	10.27	4.13	6.10

Phantom Library Simulation Results: Dose to Radiosensitive Tissues

Figure 15 plots the percent change in average dose for ODM to the breast, lung, spine, eye lens and brain tissues in the voxelized phantoms, with respect to SmartmA and AutomA. The results demonstrate a net reduction in dose for ODM in all tissue regions with the highest average dose reduction of 35.6% achieved by the breast tissue with respect to AutomA.

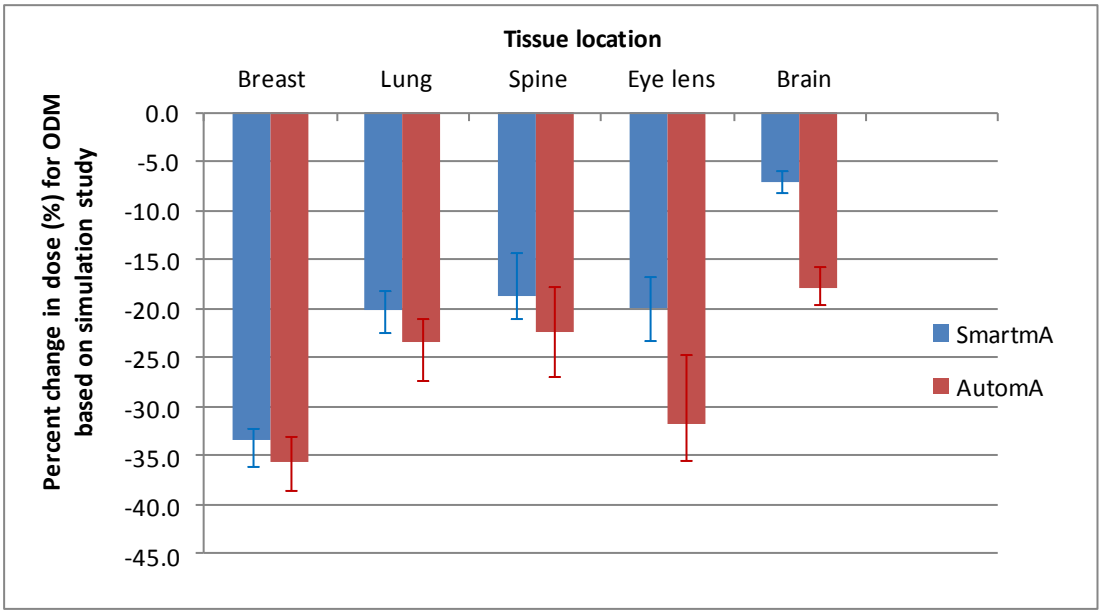

Figure 15: Percent change in dose in various tissues with respect to AutomA and SmartmA. The error bars represent standard deviation for percent change in noise across all phantoms

Phantom Library Simulation Results: Image Quality Analysis

ODM increased noise standard deviation in the brain and chest regions of all phantoms. Figure 16 below plots the percent change in noise standard deviation calculated in the chest and head regions of the reconstructed phantoms. Images reconstructed using ODM experienced an average increase in noise by 19.3% and 9.3% for chest and head phantoms, respectively as compared to SmartmA.

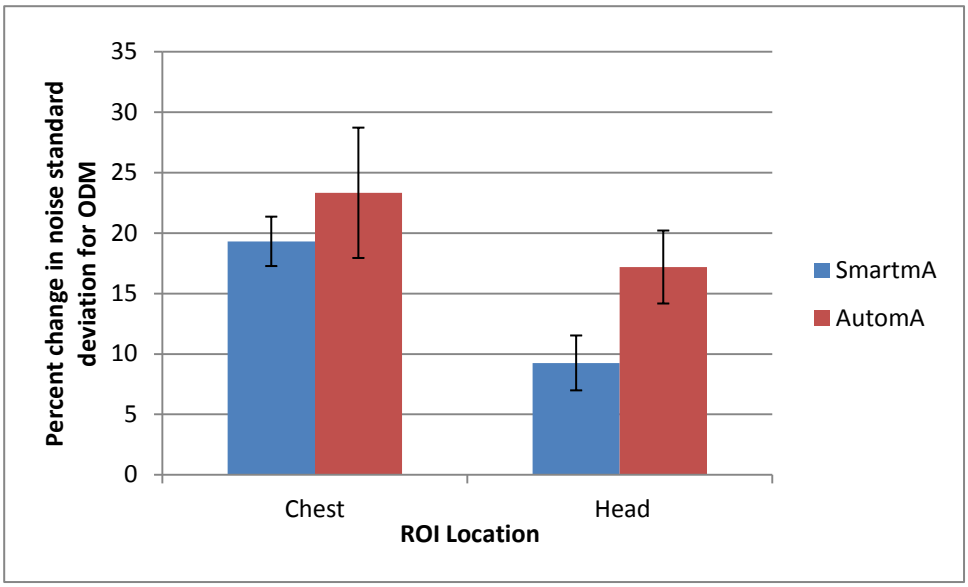

Figure 16: Percent change in noise standard deviation in chest and head regions with respect to SmartmA and AutomA. The error bars represent standard deviation for percent change in noise across all phantoms

The simulation results demonstrate that ODM changes both the organ doses and reconstructed image noise. Tube current is decreased for ODM in the anterior views without an equivalent increase in other views, thereby leading to an overall reduction in radiation dose to the phantom. Since noise is inversely proportional to the square root of dose in CT, increase in noise in expected for ODM scans. The noise could be recovered by increasing the overall mAs, which would also increase the overall dose. To determine which organs exhibit a reduction in dose with noise standard deviation held constant to AutomA and SmartmA, a cost-benefit analysis was performed by plotting relative noise versus relative dose as illustrated in figures 17 and 18. The boundary of the shaded region in the two plots represents no net benefit or detriment in dose at noise standard deviation equal to AutomA/SmartmA. The shaded area indicates a net reduction in absorbed dose for ODM at standard deviation equal to AutomA/SmartmA. The closer a data point is to the boundary, the lesser is the difference in its dose as compared to

AutomA/SmartmA. For all but five head phantoms, the eye lens exhibited a net dose reduction with respect to both AutomA and SmartmA settings at equal noise standard deviation. While ODM reduced the dose to the brain and lung tissues, these tissues would experience up to 15.2% and 13.1% dose increase respectively at noise standard deviation equal to SmartmA. All phantoms demonstrated breast dose reduction (-2.1% to -27.6%) with respect to SmartmA at equal noise standard deviation.

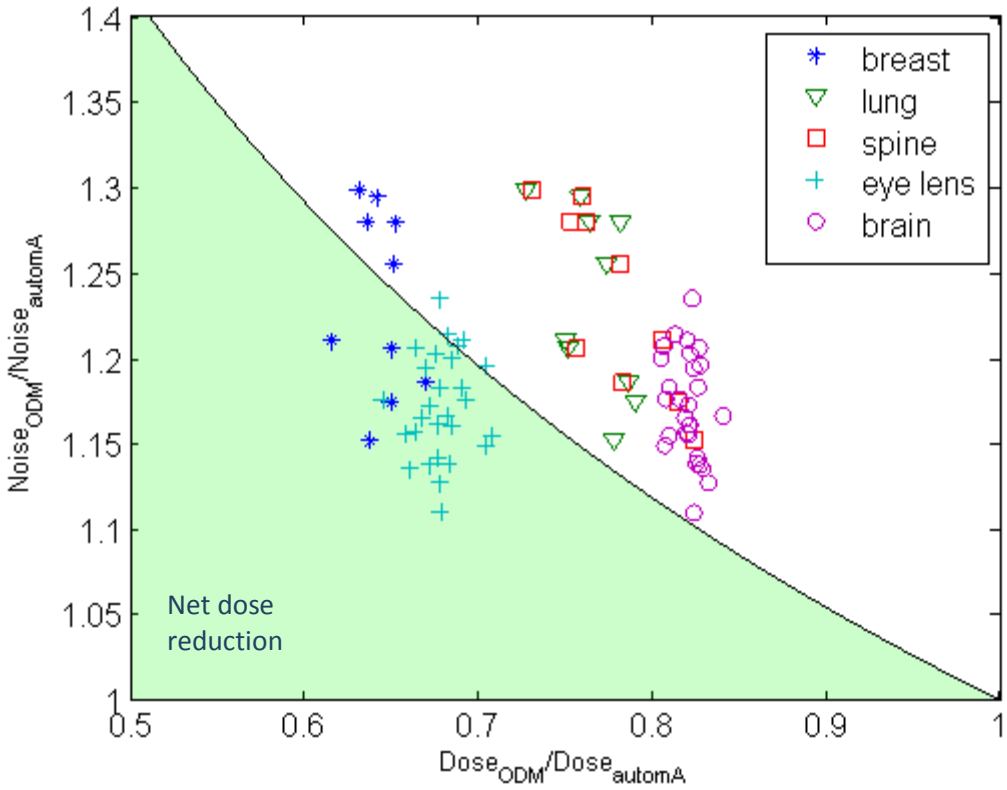

Figure 17: Relative noise versus relative dose with respect to AutomA for tissues in both head and chest phantoms

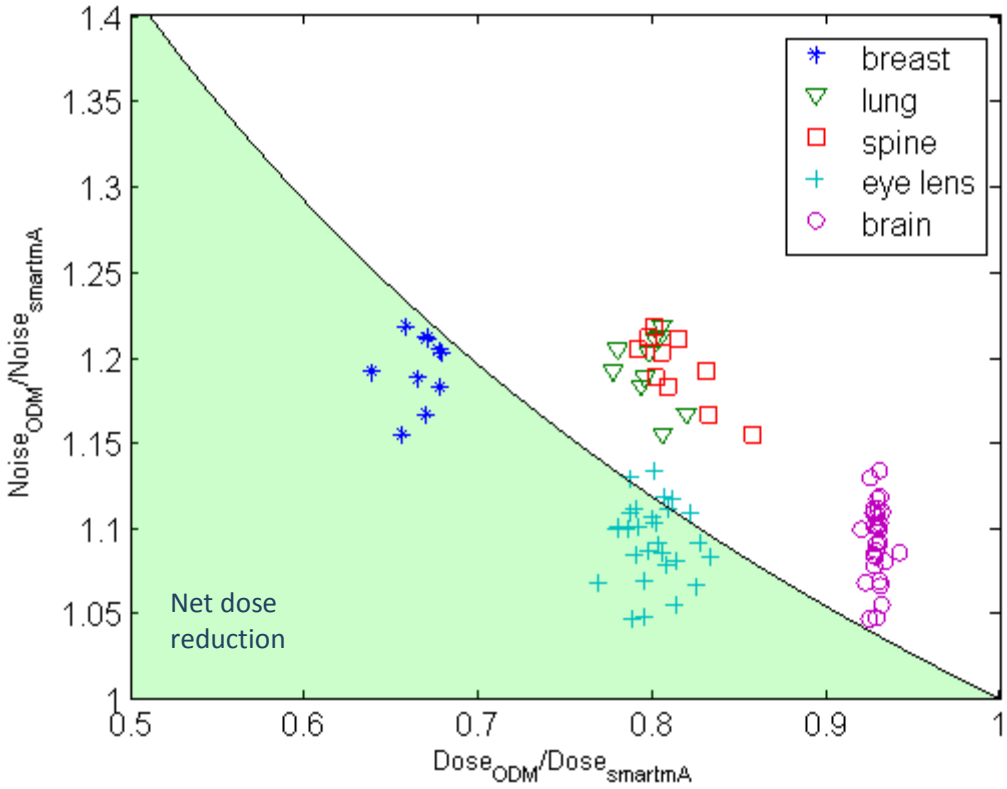

Figure 18: Relative noise versus relative dose with respect to SmartmA for tissues in both head and chest phantoms

CHAPTER 5

Discussion

The study investigated the effects of ODM on radiation dose and image quality by comparing it to TCM in the slice (AutomA) and angular (SmartmA) directions. Both experimental and simulation results demonstrated a reduction in radiation dose with ODM at all tissue locations. Since ODM focuses on further reduction in dose for the anterior views as compared to SmartmA, maximum dose reduction was observed in the anterior tissue locations such as the eye lens (16.7% to 23.1%) and breast (32.1% to 36.1%) for the head and chest scans, respectively.

ODM decreased dose in the anterior views without an increase in the posterior direction, resulting in an overall decrease in the mAs, (i.e., number of photons used to form the image). This reduction in the overall mAs by ODM also increased the noise standard deviation in the reconstructed images. Figure 17 above illustrates that a net benefit in dose reduction was achieved in all phantoms for the breast tissue with respect to SmartmA. ODM reduced dose to the eye lens in 22 of 28 phantoms (-1.2% to -12.4%), had no change in dose for one phantom, and increased dose for four phantoms (0.7% to 2.3%) with respect to SmartmA at equal noise standard deviation. All phantoms would experience a net increase in radiation dose for the lung, spine and brain regions at noise standard deviation equal to SmartmA.

Although ODM was successful in accomplishing a lower radiation dose as compared to AutomA and SmartmA TCM techniques, there was a limited degradation in the image quality measured through pixel noise in the reconstructed images. Bismuth

shields used clinically to reduce radiation dose to the breast tissue are able to provide 21% to 48% breast dose reduction [25, 40]. However, they lead to an increase in image noise, cause streak and beam hardening artifacts, and lead to increase in CT numbers for reconstructed images. A study by Wang *et al*. compares effects of global tube current reduction against bismuth shielding, where if the tube current is globally reduced to obtain the same dose as with bismuth shielding, a similar noise increase is observed in the reconstructed images without streak artifacts or errors in CT numbers [25]. Therefore, global tube reduction would be preferred over bismuth shields in this case. Similarly, if the increase in noise standard deviation caused by ODM is diagnostically acceptable, it may be preferred over a general mA reduction or bismuth shielding since ODM provides more breast dose reduction without increasing dose to other organs. In order to achieve the same breast dose, images acquired with ODM would have reduced noise as compared to the global tube current reduction method.

ODM is based on sinusoidal modulation of tube current in the angular direction along with further reduction in the anterior views, and therefore, results in a net reduction of the number of incident photons summed for all view angles. In order to reduce radiation dose without compensating for image quality, Kalender *et al.* has proposed a real-time, attenuation-based tube current modulation that aims to keep the total number of incident photons constant by modulating tube current proportional to the square root of attenuation [28, 29]. The results presented in the paper demonstrate a higher dose reduction as compared to sinusoidal modulation, while at the same time also reducing the noise or keeping it constant. A similar approach could be implemented to modify the

ODM algorithm in the near future, where the total number of incident photons is kept constant by increasing the dose for posterior views to maintain image quality.

This study compared image quality between TCM and ODM protocols through estimation of pixel standard deviation in the reconstructed images. However, this approach does not provide any information about spatial characteristics of noise, and therefore cannot be used as a reliable metric for signal detectability. To overcome this limitation of noise standard deviation, a task-based signal detectability metric could be used in the near future to compare the performance of AutomA, SmartmA and ODM protocols at various dose levels. Future analysis and assessment of image quality could also implement metrics such as noise power spectrum (NPS) and noise equivalent quanta (NEQ) that would be capable of providing insight on the frequency content of noise in CT images [35]. NPS employs Fourier transform of noise image to characterize noise power at each spatial frequency and is capable of analyzing the type of reconstruction filter used. On the other hand, NEQ (measured in photons/cm) is independent of reconstruction filter parameters and is solely affected by the amount of radiation dose (mAs) used by the scanning protocol.

Conclusion

The experimental and simulation studies on anthropomorphic and voxelized phantoms indicate that ODM has a potential to reduce dose to sensitive organs by 5 - 38% with a limited degradation in image quality measured using noise standard deviation. All phantoms with a variety of sizes (measured using body weight index) experienced a reduction in radiation dose at all tissue locations. Dose savings of up to

36.1% were achieved in the breast tissue leading to a net dose reduction in these tissues for all phantoms at equal noise standard deviation with respect to SmartmA protocols. However, additional work is required to assess modifications to the ODM algorithm such that equivalent levels of dose reduction are achieved without affecting image quality.

BIBLIOGRAPHY

[1] The American Association of Physicists in Medicine, "AAPM Response in Regards to CT Radiation Dose and its Effects," College Park, 2009.

[2] Thomson Reuters, "Author Commentaries : David Brenner on the Radiation Exposure Risk of CT Scans," Thomson Reuters, 2010.

[3] J. T. Bushberg, J. A. Seibert, J. E. M. Leidholdt and J. M. Boone, The Essential Physics of Medical Imaging, 3 ed., Lippincott Williams & Wilkins, 2011.

[4] U.S. Food and Drug Association, "Radiation-Emitting Products: What are the Radiation Risks from CT?," Silver Spring, 2009.

[5] G. Merry, "Breast cancer risks from medical imaging computed tomography and nuclear medicine among females enrolled in a large integrated health care system," Radiological Society of North America, 2012.

[6] R. J. Preston, "Radiation Protection and Tissue Reactions: An ICRP Position," U.S. Environmental Protection Agency, 2012.

[7] X. Li, E. Samei, W. Segars, G. Sturgeon, J. Colsher, G. Toncheva, T. Yoshizumi and D. Frush, "Patient-specific radiation dose and cancer risk estimation in CT: part II. Application to patients," *Medical Physics*, pp. 408-19, January 2011.

[8] L. Yu, X. Liu, S. Leng, J. M. Kofler, J. C. Ramirez-Giraldo, M. Qu, J. Christner, J. G. Fletcher and C. H. McCollough, "Radiation dose reduction in computed tomography: techniques and future perspective," *Imaging Med.*, pp. 65-84, 2009.

[9] M. K. Kalra, M. M. Maher, T. L. Toth, B. Schmidt, B. L. Westerman, H. T. Morgan and S. Saini, "Techniques and Applications of Automatic Tube Current Modulation for CT," *Radiology*, 2004.

[10] J. A. Bauhs, T. F. Vrieze, A. N. Primak, R. Bruesewitz and C. H. McCollough, "CT Dosimetry: Comparison of Measurement Techniques and Devices,"

RadioGraphics, 2008.

[11] L. S. Freudenberg and T. Beyer, "Subjective Perception of Radiation Risk," *The Journal of Nuclear Medicine,* vol. 52, no. 2, 2011.

[12] S. Agostinelli, "GEANT4 - a simulation toolkit," *Nuclear Instruments and Methods in Physics Research Section A: Accelerators, Spectrometers, Detectors and Associated Equipment,* vol. 506, no. 3, pp. 250-303, 2003.

[13] M. S. Linet, T. L. Slovis, D. L. Miller, R. Kleinerman, C. Lee, P. Rajaraman and A. d. G. Berrington, "Cancer Risks Associated With External Radiation From Diagnostic Imaging Procedures," *American Cancer Society,* vol. 62, pp. 75-100, 2012.

[14] R. F. Redberg and R. Smith-Bindman, "We Are Giving Ourselves Cancer," The New York Times, 2014.

[15] L. Hurwitz, R. Reiman, T. Yoshizumi, P. Goodman, G. Toncheva, G. Nguyen and C. Lowry, "Radiation dose from contemporary cardiothoracic multidetector CT protocols with an anthropomorphic female phantom: implications for cancer induction," *Radiology,* pp. 742-50, 2007.

[16] J. Hsieh, Computed Tomography Principles, Design, Artifacts and Recent Advances, SPIE - The International Society for Optical Engineering, 2009.

[17] L. W. Goldman, "Principles of CT and CT Technology," *Journal of Nuclear Medicine Technology,* vol. 35, no. 3, pp. 115-128, 2007.

[18] M. Blessing, M. S. Bhagwat, Y. Lyatskaya, J. R. Bellon, J. R. Hesser and P. Zygmanski, "Kilovoltage beam model for flat panel imaging system with bow-tie filter for scatter prediction and correction," *Physica Medica,* vol. 28, no. 2, pp. 134-143, 2012.

[19] F. Liu, G. Wang, W. Cong, S. Hsieh and N. Pelc, "Dynamic Bowtie for Fan-beam CT," Cornell University Library.

[20] S. E. McKenney, A. Nosratieh, D. Gelskey, K. Yang, S.-y. Huang, L. Chen and J. M. Boone, "Experimental validation of a method characterizing bow tie filters in CT scanners using a real-time dose probe," *Meical Physics,* vol. 38, no.

1406, 2011.

[21] F. Boas and D. Fleischmann, "Computed tomography artifacts: Causes and reduction techniques," *Imaging in Medicine,* vol. 4, no. 2, pp. 229-40, 2012.

[22] J.-B. Thibault, "Veo: CT Model Based Iterative-Reconstruction," GE Healthcare, Chalfont St. Giles, 2010.

[23] American Association of Physicists in Medicine, "AAPM Position Statement on the Use of Bismuth Shielding for the Purpose," AAPM, 2012.

[24] C. H. McCollough, J. Wang, R. G. Gould, S. D. and C. G. Orton, "The use of bismuth breast shields for CT should be discouraged," *Medical Physics,* vol. 39, 2012.

[25] J. Wang, X. Duan, J. A. Christner, S. Leng, Y. Lifeng and C. H. McCollough, "Radiation dose reduction to the breast in thoracic CT: Comparison of bismuth shielding, organ-based tube current modulation, and use of a globally decreased tube current," *Medical Physics,* vol. 38, 2011.

[26] M. Kalra, M. Maher and T. Toth, "Comparison of Z-axis automatic tube current modulation technique with fixed tube current CT scanning of abdomen and pelvis," *Radiology,* pp. 347-353, 2004.

[27] GE Healthcare, "GE Healthcare AutomA / SmartmA Theory," 2008. [Online]. Available: http://www.gehealthcare.com/usen/education/tip_app/docs/AutomA-SmartmA%20Theory.pdf.

[28] M. Gies, W. A. Kalender, H. Wolf and C. Suess, "Dose reduction in CT by anatomically adapted tube current modulation. I. Simulation studies," *Medical Physics,* vol. 26, no. 11, pp. 2235-47, 1999.

[29] W. A. Kalender, H. Wolf and C. Suess, "Dose reduction in CT by anatomically adapted tube current modulation. II. Phantom measurements," *Medical Physics,* vol. 26, no. 11, pp. 2248-53, 1999.

[30] E. Angel, N. Yaghmai, C. M. Jude, J. J. DeMarco, C. H. Cagnon, J. G. Goldin, C. H. McCollough, A. N. Primak, D. D. Cody, D. M. Stevens and M. F. McNitt-

Gray, "Dose to Radiosensitive Organs During Routine Chest CT: Effects of Tube Current Modulation," *American Journal of Roentgenology,* vol. 193, no. 5, pp. 1340-1345, November 2009.

[31] L. Hurwitz, T. Yoshizumi, P. Goodman, R. Nelson, G. Toncheva, G. Nguyen, C. Lowry and C. Anderson-Evans, "Radiation dose savings for adult pulmonary embolus 64-MDCT using bismuth breast shields, lower peak kilovoltage, and automatic tube current modulation," *American Journal of Roentenology,* vol. 192, no. 1, pp. 244-53, January 2009.

[32] J. H. Hubbell and S. M. Seltzer, "Tables of X-Ray Mass Attenuation Coefficients," National Institute of Standards and Technology, 1996.

[33] J. Bond, D. Frush, E. Samei and W. P. Segars, "Simulation of anatomical texture in voxelized XCAT phantoms," *Physics of Medical Imaging,* 19 March 2013.

[34] D. Zhang, A. S. Savandi, J. J. Demarco, C. H. Cagnon, E. Angel, A. C. Turner, D. D. Cody, D. M. Stevens, A. N. Primak and C. H. McCollough, "Variability of surface and center position radiation dose in MDCT: Monte Carlo simulations using CTDI and anthropomorphic phantoms," *Medical Physics,* vol. 36, pp. 1025-1038, 2009.

[35] K. L. Boedeker, V. N. Cooper and M. F. McNitt-Gray, "Application of the noise power spectrum in modern diagnostic MDCT: part I. Measurement of noise power spectra and noise equivalent quanta," *Physics in Medicine and Biology,* vol. 52, pp. 4027-4046, 2007.

[36] S. e. a. McKenny, "Experimental validation of a method characterizing bow tie filters in CT scanners using a real-time dose probe," *Medical Physics,* vol. 38, pp. 1406-1415, 2011.

[37] "ICRP Statement on Tissue Reactions / Early and Late Effects of Radiation in Normal Tissues and Organs – Threshold Doses for Tissue Reactions in a Radiation Protection Context," International Commission of Radiological Protection, 2012.

[38] X. Duan, J. Wang, J. A. Christner, S. Leng, K. L. Grant and C. H. McCollough, "Dose Reduction to Anterior Surfaces With Organ-Based Tube-Current Modulation: Evaluation of Performance in a Phantom Study," *American*

Journal of Roentgenology, vol. 197, pp. 689-695, 2011.

[39] C. Yamauchi-Kawaura, M. Yamauchi, K. Imai, M. Ikeda and T. Aoyama, "Image quality and age-specific dose estimation in head and chest CT examinations with organ-based tube-current modulation," *Radiation Protection Dosimetry,* vol. 157, pp. 193-205, 2013.

[40] S. A. Vollmar and W. A. Kalender, "Reduction of dose to the female breast in thoracic CT: a comparison of standard-protocol, bismuth-shielded, partial and tube-current-modulated CT examinations," *Eur Radiol,* vol. 18, pp. 1674-1682, 2008.

APPENDIX

Code for segmenting XCAT voxelized phantoms

```
%%%
```

```
    fid=fopen(filename,'r');
    A_raw = fread(fid,'uint8');
    A = round(10000.*A_raw)./10000;
%    scan linear attentuation coefficient (1/pixel) values:
%    Body (water)    =       0.0127
%    Muscle          =       0.0132
%    Adipose (fat)   =       0.0117
%    Lung            =       0.0038
%    Spine Bone      =       0.0153
%    Rib Bone        =       0.0185
%    Blood           =       0.0133
%    Heart           =       0.0132
%    Kidney          =       0.0132
%    Liver           =       0.0133
%    Lymph           =       0.0130
%    Pancreas        =       0.0131
%    Spleen          =       0.0133
%    Intestine       =       0.0130
%    Skull           =       0.0165
%    Cartilage       =       0.0138
%    Brain           =       0.0131


%store in img_set(num_rows,num_cols,num_slices)
```

```
pix_num = 1;
for slice_num=1:1:num_slices
    disp(['slice: ',num2str(slice_num)]);
    for i=1:num_rows
        for j=1:num_cols
            if A(pix_num) == 0
                img_set(i,j,slice_num) = 0; %air

            elseif A(pix_num) == 1
                img_set(i,j,slice_num) = 7; %body (water)

            elseif A(pix_num) == 14 || A(pix_num) == 15 ||
A(pix_num) == 79
                img_set(i,j,slice_num) = 1; %lung

            elseif A(pix_num) >= 71 && A(pix_num) <= 78
                img_set(i,j,slice_num) = 5; %blood

            elseif A(pix_num) == 2 || A(pix_num) == 64
                img_set(i,j,slice_num) =3; %muscle

            elseif A(pix_num) ==  18 || A(pix_num) ==  41
|| A(pix_num) ==  42 || A(pix_num) ==  28 || A(pix_num) ==
66 || A(pix_num) ==  47 || A(pix_num) ==  68 || A(pix_num)
```

```
==  16 || A(pix_num) == 19 || A(pix_num) == 21 ||
A(pix_num) == 61 || A(pix_num) == 70 || A(pix_num) == 63 ||
A(pix_num) == 60 || A(pix_num) ==  24 || A(pix_num) ==  26
                img_set(i,j,slice_num) = 2; %soft tissue

            elseif A(pix_num) == 80
                img_set(i,j,slice_num) = 4; %glandular
breast

            elseif A(pix_num) == 4 || A(pix_num) == 5 ||
A(pix_num) == 6
                img_set(i,j,slice_num) = 6; %bone

            elseif A(pix_num) == 3
                img_set(i,j,slice_num) = 8; %cartilage

            else
                %img_set(i,j,slice_num) = 2; %soft tissue
                disp('Nothing');
                disp(A(pix_num));
            end
            pix_num=pix_num+1;
        end
    end
```

```
end


%% Writing to output files
z_coordinate = 0.00;
z_coordinate_end = 1; %mm
for i=1:num_slices
    output_filename = [num2str(i) '.g4'];
    fid_out = fopen(output_filename, 'w');
    disp(i);
    str1 = '9';
    str2 = '0 Air';
    str3 = '1 Lung';
    str4 = '2 SoftTissue'; %brain
    str5 = '3 Muscle';
    str6 = '4 glandularBreast';
    str7 = '5 Blood';  %skull
    str8 = '6 Bone'; %muscle and eye
    str9 = '7 Water';
    str10 = '8 Cartilage';
    str12 = '512 512 1';
    str13 = '-256.000 256.000';
    str14 = '-256.000 256.000';
    str15 = num2str(z_coordinate);
    str16 = num2str(z_coordinate_end);
```

```
    z_coordinate_end = z_coordinate_end + 1;
    z_coordinate = z_coordinate + 1;
    fprintf(fid_out,
'%s\r\n%s\r\n%s\r\n%s\r\n%s\r\n%s\r\n%s\r\n%s\r\n%s\r\n%s\r
\n%s\r\n%s\r\n%s\r\n%s %s\r\n',
str1,str2,str3,str4,str5,str6,str7,str8,str9,str10,str12,st
r13,str14,str15,str16);

    %write pixel values to file
    for row=1:1:num_rows
        for col=1:1:num_cols
            fprintf(fid_out,'%s
',num2str(img_set(row,col,i)));
        end
    end
    fclose(fid_out);

end
fclose(fid);

foldername = ['geantino_chest_',phantom_name,'.tgz'];
tar(foldername,'*.g4');
```

Code for calculating total dose deposition using results from Monte Carlo dose simulations

```
%%%%%%%%%%%%%%%%%%%%%%%%%%%%%%%%%%%%%%%%%%%%%%%%%%%%%%%%%%%
%%%%%%%%%%%%%%%%
%Author: Diksha Gandhi
%Last modified: 03/03/2014
%Description: This code calculates total dose deposition
for AutomA,
%SmartmA and ODM settings using dose output files from
GEANT4 Monte Carlo
%simulations
%%%%%%%%%%%%%%%%%%%%%%%%%%%%%%%%%%%%%%%%%%%%%%%%%%%%%%%%%%%
%%%%%%%%%%%%%%%%

clear all;

%Input parameters
phantom = 'f140';
scan_type = 'chest';
num_views = 492;
num_rots = 6;

dose_ama=zeros(33,num_rots);
dose_ama(:,1)=0;
```

```
dose_odm=zeros(33,num_rots);
dose_odm(:,1)=0;
dose_sma=zeros(33,num_rots);
dose_sma(:,1)=0;
input_set = ['dose_chest',num2str(phantom),'_ama.tgz'];
maTable_set = ['maTable_chest_',num2str(phantom),'.tgz'];
%untar(input_set);
%untar(maTable_set);

for rot = 0
    ma_a = ['maTable_chest_ama',num2str(rot),'.dat'];
    ma_s = ['maTable_chest_sma',num2str(rot),'.dat'];
    ma_o = ['maTable_chest_odm',num2str(rot),'.dat'];
    ma_ama = load(ma_a);
    ma_sma = load(ma_s);
    ma_odm = load(ma_o);
    x1 = 0:360/968:360;
    x2 = 0:360/492:360;
    ma_ama_492 = interp1(x1(1:968),ma_ama,x2(1:492));
    ma_sma_492 = interp1(x1(1:968),ma_sma,x2(1:492));
    ma_odm_492 = interp1(x1(1:968),ma_odm,x2(1:492));
    rel_odm = ma_odm_492./ma_ama_492;
    rel_sma = ma_sma_492./ma_ama_492;
```

```
    for view = 0:num_views-1

out=load(['dose_',num2str(view),'_',num2str(rot),'.out']);
        out_odm = out;
        out_sma = out;
        if size(out_odm)~=[0,0]
            out_odm(:,2) =
out_odm(:,2).*rel_odm(((view)+1));
            out_sma(:,2) =
out_sma(:,2).*rel_sma(((view)+1));
        end
        for p=1:size(out,1)

dose_ama(out(p,1),rot+1)=out(p,2)+dose_ama(out(p,1),rot+1);

dose_odm(out_odm(p,1),rot+1)=out_odm(p,2)+dose_odm(out_odm(
p,1),rot+1);

dose_sma(out_sma(p,1),rot+1)=out_sma(p,2)+dose_sma(out_sma(
p,1),rot+1);

%delete(['dose_',num2str(view),'_',num2str(rot),'.out']);
        end
    end
```

```
end



dose_total(:,1) = sum(dose_ama,2);

dose_total(:,2) = sum(dose_sma,2);

dose_total(:,3) = sum(dose_odm,2);
```